Monthly Notices
of the
ROYAL ASTRONOMICAL SOCIETY

MNRAS **484,** 2674–2683 (2019)
Advance Access publication 2019 January 16

doi:10.1093/mnras/sty3430

A discontinuity in the $T_{\rm eff}$–radius relation of M-dwarfs

Markus Rabus,[1,2,3,4★] Régis Lachaume,[1,2] Andrés Jordán,[1,5] Rafael Brahm,[1,5] Tabetha Boyajian,[6] Kaspar von Braun,[7] Néstor Espinoza,[2] Jean-Philippe Berger,[8] Jean-Baptiste Le Bouquin[9] and Olivier Absil[10]

[1]*Instituto de Astronomía, Facultad de Física, Pontificia Universidad Católica de Chile, Casilla 306, Santiago 22, Chile*
[2]*Max-Planck-Institut für Astronomie, Königstuhl 17, D-69117 Heidelberg, Germany*
[3]*Las Cumbres Observatory Global Telescope, 6740 Cortona Dr., Suite 102, Goleta, CA 93111, USA*
[4]*Department of Physics, University of California, Santa Barbara, CA 93106-9530, USA*
[5]*Millennium Institute for Astrophysics, Chile*
[6]*Department of Physics and Astronomy, Louisiana State University, 202 Nicholsom Hall, Baton Rouge, LA 70803, USA*
[7]*Lowell Observatory, 1400 W. Mars Hill Road, Flagstaff, AZ 86001, USA*
[8]*Institut de Planétologie et d'Astrophysique de Grenoble, Observatoire de Grenoble, 38000 Grenoble, France*
[9]*Department of Astronomy, University of Michigan, 1085 S. University, Ann Arbor, MI 48109, USA*
[10]*STAR Institute, Université de Liège, 19c Allée du Six Août, B-4000 Liège, Belgium*

Accepted 2018 November 30. Received 2018 November 30; in original form 2018 July 17

ABSTRACT

We report on 13 new high-precision measurements of stellar diameters for low-mass dwarfs obtained by means of near-infrared long-baseline interferometry with PIONIER at the Very Large Telescope Interferometer. Together with accurate parallaxes from *Gaia* DR2, these measurements provide precise estimates for their linear radii, effective temperatures, masses, and luminosities. This allows us to refine the effective temperature scale, in particular towards the coolest M-dwarfs. We measure for late-type stars with enhanced metallicity slightly inflated radii, whereas for stars with decreased metallicity we measure smaller radii. We further show that *Gaia* DR2 effective temperatures for M-dwarfs are underestimated by ∼8.2 per cent and give an empirical M_G–$T_{\rm eff}$ relation that is better suited for M-dwarfs with $T_{\rm eff}$ between 2600 and 4000 K. Most importantly, we are able to observationally identify a discontinuity in the $T_{\rm eff}$–radius plane, which is likely due to the transition from partially convective M-dwarfs to the fully convective regime. We found this transition to happen between 3200 and 3340 K, or equivalently for stars with masses ≈0.23 $M_\odot$. We find that in this transition region the stellar radii are in the range from 0.18 to 0.42 $R_\odot$ for similar stellar effective temperatures.

Key words: techniques: interferometric – stars: fundamental parameters – stars: late-type – stars: low-mass.

1 INTRODUCTION

Low-mass dwarfs are the most numerous stars in the Universe and understanding them is thus clearly an important endeavour. Beyond their own interest, investigations by Bonfils et al. (2013), Dressing & Charbonneau (2013), and Kopparapu (2013) have shown that M-dwarfs may be the most abundant planet hosts in the Milky Way as well. The estimation of parameters and properties of an exoplanet are intimately connected to the stellar host, e.g. the stellar mass determines the measured semi-amplitude for radial velocity observations and hence influences the mass estimate of the planet. In the case of transiting extrasolar planets, their physical radii can be measured from the transit shape if the radii of the stellar hosts are known. In addition, the stellar radius and effective temperature are linked to the planet's surface temperature and the location of the habitable zone. All of these examples illustrate how important stellar astrophysical properties are for the characterization of exoplanets in general. M-dwarfs are attractive targets to search for transiting exoplanets not only due to their numbers, but also due to the fact that for a given planetary size the transit depth is deeper around low-mass stars due to their smaller sizes. Also, the habitable zone around these stars is closer, resulting in shorter periods that make detection easier. Indeed, one of the main drivers for the upcoming *TESS* mission (Ricker et al. 2014) is to detect transiting exoplanets around low-mass stars.

A fundamental stellar property is the radius and for low-mass stars its estimation has been done mostly through stellar models. Fortunately, considerable improvements in interferometric

★ E-mail: mrabus@astro.puc.cl

observation techniques allow us now to obtain stellar parameters such as the stellar radius directly. However, these measurements become more difficult as we go to cooler dwarf stars due to their inherently lower luminosity and smaller radii. Measured angular diameters of M-dwarfs are generally close to the current baseline limit of available interferometers. Up to now, extensive interferometric observations on M-dwarf stars have been done mainly from the Northern Hemisphere with the CHARA array (Berger et al. 2006; von Braun et al. 2011; Boyajian et al. 2012a; von Braun et al. 2014) and a few with the VLT-Interferometer (VLTI) from the South (Ségransan et al. 2003; Demory et al. 2009). These interferometric direct measurements showed a discrepancy with the parameters measured indirectly (Boyajian et al. 2012b). The work of Boyajian et al. (2012b) found in particular large disagreements for low-mass stars, where the radii measured by interferometers were more than 10 per cent larger than the ones based on models from Chabrier & Baraffe (1997). Likewise, Kesseli et al. (2018) found that this inflation of the M-dwarf radii extends down to the fully convective regime with a discrepancy of 13–18 per cent.

This discrepancy affects, in turn, other stellar parameters like surface temperature ($T_{\rm eff}$), gravities ($\log g$), masses, luminosities, and eventually also possible planetary parameters. Therefore, it is important to observe and re-evaluate the properties of more M-dwarf stars with interferometric observations, particularly towards the later spectral types that have not been extensively studied at all.

Theoretical stellar evolution models for low-mass stars predict a transition into the fully convective regime to occur somewhere between $0.2\,M_{\odot}$ (Dorman, Nelson & Chau 1989) and $0.35\,M_{\odot}$ (Chabrier & Baraffe 1997), depending on the underlying stellar model. For partially convective stars, the stellar structure is Sun-like, having a radiative zone and a convective envelope. The only previous observational indications for this transition in late-type stars are based on observations of magnetic fields and measurements of stellar rotational periods. Browning (2008) showed that stars whose convective region extends to the core have strong large-scale magnetic fields and, in fact, we have observational evidence that the fraction of M-dwarfs with strong magnetic fields on a large scale is higher for mid- to late-type M-dwarfs than for early-type ones (Donati et al. 2008). On the other hand, Wright & Drake (2016) showed that rotation-dependent dynamos are very similar in both partially and fully convective stars. Irwin et al. (2011) and Newton et al. (2016) measured rotational spin-velocities of M-stars. The authors found two divergent populations of faster and slower rotators in the fully convective mass regime, which makes rotation measurements difficult to use in the determination of whether a late-type star is fully convective. Moreover, the rotation of fully convective stars depends on both age and mass. All former indications of fully convective stars have been done indirectly and are not unambiguous.

In this work we present directly measured physical parameters for a sample of 13 low-mass stars using observations with the VLTI. These observations are used to probe the transition between the partially and fully convective regimes and to identify the dependence of the stellar radii on other stellar properties. The paper is structured as follows. In Section 2 we lay out the observational details. In Section 3 we detail how we estimated the stellar physical parameters. Finally, we discuss the implication of the measured stellar parameters on stellar evolution and structure models in Section 4 and we conclude in Section 5.

2 OBSERVATIONS AND DATA REDUCTION

2.1 PIONIER observations

Our target sample is compiled from a list of M-dwarfs within ∼15 pc (so the stars are resolved within the given VLTI baseline) and with H-band magnitudes <7 (so that fringes will be easily visible and we can obtain a good signal-to-noise ratio).

In order to measure the angular diameter of our sample stars, we used the VLTI/PIONIER interferometer (Le Bouquin et al. 2011). PIONIER is an integrated optics four-beam combiner operating at the near-infrared wavelength range. We used the auxiliary telescopes (ATs) in a A1-G1-K0-J3 quadruplet configuration. This configuration gave us the longest VLTI baseline available (from 57 m between the stations K0 and J3, up to 140 m between A1 and J3) and we used the Earth's rotation to further fill the (u, v) plane.

We observed our sample with a three-channel spectral dispersion (SMALL mode) whenever possible. In cases where this was not possible, due to low coherence time on a given night or the relative faintness of the target, we observed without spectral dispersion (FREE mode). Similarly, the number of scan steps were adjusted according to the objects' brightness and atmospheric conditions. As our sample stars were not too bright we were able to use the fast Fowler readout mode for all of our observations.

Our observing strategy was to bracket each science frame (SCI) with a calibrator star (CAL), observed with the same set-up as the science object. The calibrators are chosen to be mostly point-like nearly unresolved stars (van Belle & van Belle 2005), so the uncertainties in their diameter will not influence our targets, but we also included calibrators with known diameter for verification purposes. We also made sure that the visibility precision of our calibrators was below 1 per cent. In order to search for suitable calibrators, we used the ASPRO2-tool and SearchCal.[1] For each science target, we repeated around 11 times a CAL-SCI-CAL block and in each block we used different calibrator stars. The same target was also observed on different nights. This strategy helped us to beat down the systematic noise from the instrument and atmosphere. We reduced our observed raw fringes to calibrated visibilities and closure phases with a modified version of the PIONIER data reduction software (*PNDRS*; described in Lachaume et al. 2019).

2.2 Calibrated visibilities and angular diameters

Our modified data reduction with *PNDRS* is fully described in detail in a publication by Lachaume et al. (2019), where we also show a rigorous analysis of the interferometric measurement errors. Here we will give only a brief summary of the data reduction process and we refer interested readers to Lachaume et al. (2019) for more details on the data analysis. In the first step we calibrate the detector frames. This was done by dark correcting the detector data and from the kappa matrix we calibrated the transmission of the respective baseline. Finally, we used frames illuminated by an internal light source to calibrate the wavelength. Basically, these calibrated frames will allow us to obtain the raw visibilities, which are in turn the product of true visibilities and the system transfer function. The system transfer function characterizes the response of the interferometer as a function of spatial frequency and in order to get the true visibilities, it needs to be estimated by using calibrator stars. Assuming that all our calibrator stars

[1] http://www.jmmc.fr/aspro_page.htm

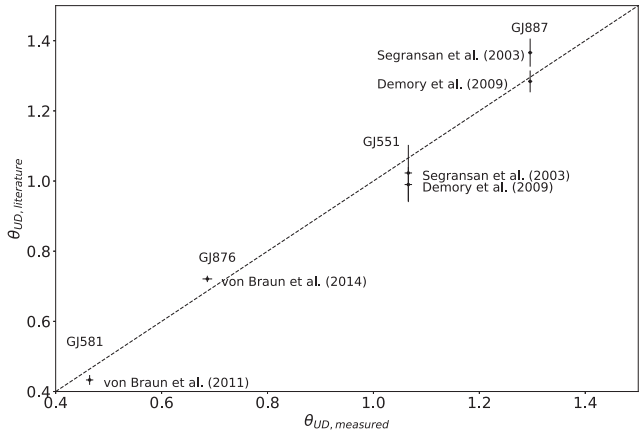

Figure 1. Our angular diameters $\theta_{\rm UD}$ compared to literature values. We find good agreement between our measurements and the literature.

have well-known true visibilities, i.e. an unresolved calibrator has a known visibility of unity and a resolved star has a known diameter, either measured or from spectral typing. By further assuming a smooth transfer function, in theory this would allow us to calibrate our raw visibilities. Nevertheless, uncertainties in the assumed calibrators' diameters can impact all observations in a sequence due to systematic errors in the transfer function estimate (Lachaume et al. 2019, and references therein). Further errors can be introduced through systematic uncertainties in the absolute wavelength calibration (Gallenne et al. 2018) and by several other random effects that will affect the different spectral channels in a similar or imbalanced manner, like e.g. atmospheric jitter or flux variations between the arms of the interferometer. In order to account for the correlation effects in our observations, we apply a bootstrap method as described in Lachaume et al. (2019) and Lachaume, Rabus & Jordán (2014).

Generally, in a bootstrap one resamples several times new data sets from the empirical data itself by replacing parts of the original data. For each candidate, we started by picking randomly interferograms out of the parent population of $\sim 10^2$ interferograms. These interferograms are reduced and averaged to a single data set that corresponds to the raw visibility. As mentioned before, uncertainties in the calibrators' diameter can cause correlated errors. Therefore, we choose arbitrarily a calibrator with a diameter, drawn randomly from a Gaussian distribution centred on the catalogued diameter and with a width corresponding to the error bars. We used 6 to 18 data sets and calibrators to replace the original data and to calculate the system transfer function and calibrated visibilities. We repeat this procedure to obtain 5000 bootstrap realizations. These calibrated visibilities were fitted with a uniform disc ($\theta_{\rm UD}$) model to obtain a distribution of angular diameters for each star observed. In Fig. 1 we compare some of our measured $\theta_{\rm UD}$ with the ones available in the literature. We find a good agreement between our measurements and the literature values.

3 ESTIMATING THE PHYSICAL PARAMETERS FROM INTERFEROMETRY

3.1 Calculation of the stellar radius

The limb darkened disc $\theta_{\rm LD}$ is usually obtained by fitting directly a limb darkened disc model to the squared visibilities, assuming a certain limb darkening law and coefficient. Generally, a linear limb darkening law is assumed and tabulated values are used for the coefficients (see e.g. von Braun et al. 2011; Boyajian et al. 2012b; von Braun et al. 2014). We note that while $\theta_{\rm UD}$s are independent of stellar models, photospheric diameters, $\theta_{\rm LD}$s depend on stellar models as the limb-darkening coefficient are derived from them. However, the impact on the radius estimate by the limb-darkening in the near-infrared is small (2–4 per cent) and it is mostly dominated by the angular diameter measurement uncertainties and systematics.

In order to estimate the $\theta_{\rm LD}$, we used the $\theta_{\rm UD}$–$\theta_{\rm LD}$ relation from Hanbury Brown et al. (1974):

$$\theta_{\rm LD}(\lambda) = \theta_{\rm UD}\sqrt{\frac{1-\frac{1}{3}\mu(\lambda, T_{\rm eff}, \log g)}{1-\frac{7}{15}\mu(\lambda, T_{\rm eff}, \log g)}}, \quad (1)$$

where $\theta_{\rm UD}$ is the angular diameter we obtained from the calibrated visibilities and μ_λ is the linear limb darkening coefficient as function of wavelength, $T_{\rm eff}$ and $\log g$. Rather than using tabulated coefficient, we calculated a grid of limb darkening coefficients following Espinoza & Jordán (2015) corresponding to the atmosphere grid with $T_{\rm eff}$ in the range of 2300–4500 K, $\log g$ in the range of 4.0–6.0, and a fixed metallicity of 0.0. This allows us to have a conformity with the grid that will be used in Section 3.3. As filter transmission function of PIONIER, we used a top hat function between 1.5 and 1.8 μm.

3.2 $T_{\rm eff}$ estimate

The measured diameters can be related to the effective temperature by

$$T_{\rm eff} = \sqrt[4]{\frac{4F_{\rm bol}}{\sigma\theta_{\rm LD}}}, \quad (2)$$

where $F_{\rm bol}$ is the bolometric flux (obtained by e.g. fitting the spectral energy distribution with literature photometry to spectral templates), $\theta_{\rm LD}$ is the limb darkened angular diameter, and σ is the Stefan–Boltzmann constant.

3.3 Bolometric flux estimate

In order to estimate the bolometric flux, we started by using the PHOENIX atmosphere models from Husser et al. (2013) to create a grid of synthetic photometric points for filters with available photometric observations of our sample stars. Their models are defined in the wavelength range from 0.05 to 5.5 μm. Our flux model grid runs $T_{\rm eff}$ from 2300 to 4500 K, $\log g$ between 4.0 and 6.0 dex, and for a fixed metallicity of 0.0 dex. The flux was integrated over the respective band and convolved with the filter profiles from Mann & von Braun (2015). We linearly interpolated this grid of synthetic flux in-between. The bolometric flux $F_{\rm bol}$ of a given star is then defined as

$$F_{\rm bol} = \int_0^{+\infty} F_{\rm model}(\lambda, T_{\rm eff}, \log g)\frac{R_\star^2}{d^2}{\rm d}\lambda, \quad (3)$$

where $R_\star$ is the stellar radius and d is the distance.

3.4 Multinest fitting for $T_{\rm eff}$, $R_\star$, and $L_\star$

We first collected observed fluxes for our stars using the VizieR photometric query. To these observed fluxes, we fitted the model grid using the *PYMULTINEST* code (Buchner et al. 2014). This program is a PYTHON code for multimodal nested sampling technique (Skilling

Table 1. Final parameter estimates obtained through multimodal nested sampling technique (see Section 3.4 for details).

Star name	θ_{UD} (mas)	θ_{LD} (mas)	μ_λ	F_{bol} (10^{-8} erg s^{-1} cm^{-2})	$R_\star$ ($R_\odot$)	Parallax (mas)	Calculated T_{eff} (K)
GJ 1	0.794 ± 0.005	0.812 ± 0.005	0.290	3.751 ± 0.072	0.379 ± 0.002	230.133 ± 0.059	3616 ± 14
GJ 273	0.763 ± 0.010	0.783 ± 0.010	0.335	2.288 ± 0.118	0.320 ± 0.005	262.961 ± 1.387	3253 ± 39
GJ 406	0.562 ± 0.020	0.582 ± 0.020	0.449	0.563 ± 0.044	0.159 ± 0.006	394.867 ± 7.893	2657 ± 20
GJ 447	0.524 ± 0.029	0.540 ± 0.029	0.365	1.103 ± 0.091	0.196 ± 0.010	296.309 ± 0.069	3264 ± 24
GJ 551	1.066 ± 0.007	1.103 ± 0.007	0.422	2.866 ± 0.210	0.154 ± 0.001	768.500 ± 0.203	2901 ± 68
GJ 581	0.464 ± 0.007	0.476 ± 0.007	0.324	0.967 ± 0.039	0.322 ± 0.005	158.747 ± 0.051	3366 ± 28
GJ 628	0.644 ± 0.014	0.661 ± 0.014	0.335	1.882 ± 0.068	0.306 ± 0.007	232.209 ± 0.063	3372 ± 12
GJ 674	0.720 ± 0.037	0.737 ± 0.037	0.318	2.443 ± 0.232	0.360 ± 0.018	219.800 ± 0.047	3409 ± 25
GJ 729	0.625 ± 0.020	0.642 ± 0.020	0.345	1.370 ± 0.096	0.205 ± 0.006	336.121 ± 0.064	3162 ± 30
GJ 832	0.794 ± 0.010	0.814 ± 0.010	0.325	3.359 ± 0.113	0.435 ± 0.005	201.407 ± 0.043	3512 ± 23
GJ 876	0.686 ± 0.009	0.705 ± 0.009	0.342	1.902 ± 0.058	0.354 ± 0.005	213.866 ± 0.078	3275 ± 18
GJ 887	1.297 ± 0.005	1.328 ± 0.004	0.323	10.916 ± 0.657	0.470 ± 0.001	304.219 ± 0.044	3692 ± 57
Literature stars							
GJ 176	0.442 ± 0.020	0.452 ± 0.020	0.306	1.274 ± 0.099	0.460 ± 0.020	105.565 ± 0.069	3700 ± 45
GJ 205	0.904 ± 0.003	0.924 ± 0.003	0.283	6.140 ± 0.400	0.566 ± 0.002	175.430 ± 0.069	3835 ± 69
GJ 411	1.380 ± 0.013	1.412 ± 0.013	0.301	10.514 ± 0.515	0.387 ± 0.004	392.630 ± 0.675	3547 ± 40
GJ 436	0.405 ± 0.013	0.415 ± 0.013	0.321	0.800 ± 0.053	0.436 ± 0.013	102.497 ± 0.093	3436 ± 33
GJ 526	0.807 ± 0.013	0.824 ± 0.013	0.287	4.134 ± 0.183	0.482 ± 0.008	183.983 ± 0.051	3677 ± 30
GJ 649	0.472 ± 0.012	0.483 ± 0.012	0.294	1.329 ± 0.072	0.539 ± 0.013	96.314 ± 0.031	3619 ± 25
GJ 687	0.830 ± 0.013	0.850 ± 0.013	0.317	3.380 ± 0.145	0.416 ± 0.007	219.781 ± 0.033	3443 ± 29
GJ 699	0.917 ± 0.005	0.941 ± 0.005	0.342	3.176 ± 0.120	0.185 ± 0.001	548.358 ± 1.513	3221 ± 32
GJ 809	0.698 ± 0.008	0.715 ± 0.008	0.314	3.341 ± 0.148	0.541 ± 0.006	142.033 ± 0.030	3743 ± 39
GJ 880	0.716 ± 0.004	0.736 ± 0.004	0.357	3.468 ± 0.084	0.544 ± 0.003	145.610 ± 0.038	3724 ± 23

2004; Feroz & Hobson 2008). Our log-likelihood function is

$$\log \mathcal{L} = -\sum_{i=1}^{N_{phot}} \left[\frac{(F_{i,obs} - F_{i,mod})^2}{2\sigma_i^2} - \log \frac{1}{\sigma_i \sqrt{2\pi}} \right], \quad (4)$$

where $F_{i,obs}$ is the observed flux in a given filter i, $F_{i,mod}$ is the synthetic flux in that filter obtained from the atmosphere models, and σ_i is the corresponding measurement error of the observed flux. The sum goes over the N_{phot} photometric measurements of a given star.

Our priors are T_{eff}, $\log g$, distance, and angular diameter θ_{UD}. All our priors were drawn from a normal distribution centred at the literature value and with a dispersion corresponding to the respective error. We further repeated this process using M-dwarfs with measured diameters from von Braun et al. (2012), Boyajian et al. (2012a), and von Braun et al. (2014). Our final parameter estimates are shown in Table 1. We compare our values with the ones from Mann et al. (2015) in Fig. 2 and find good agreement with a mean difference of 3 per cent for all three parameters (from top to bottom: radius, F_{bol}, T_{eff}). In the same Fig. 2 (bottom plot), we further compare our effective temperatures with the ones obtained by Neves et al. (2014) through spectral type classification using optical spectroscopy and from *Gaia* DR2 using Apsis (Andrae et al. 2018). In the latter cases the relative difference for T_{eff} is generally higher, with a mean difference of 5.4 and −8.2 per cent, respectively. Therefore, spectral typing of M-dwarfs in the optical wavelength range generally overestimates T_{eff}s, whereas *Gaia* DR2 T_{eff}s are considerably underestimated.

3.5 Mass estimates

The mass cannot be measured directly from interferometry. Therefore, we make use of a fully empirical model-independent mass–luminosity relation (MLR) from Benedict et al. (2016) and Mann et al. (2018). In both cases we use their calibration relations in *K*-band; therefore for all our stars we collected SAAO *K*-band magnitudes from Koen et al. (2010) and *Ks*-band magnitudes from Mann et al. (2015) and Cutri et al. (2003). The corresponding magnitudes are given in Table 2. The SAAO *K*-band magnitudes were transformed to 2MASS Ks using the transformation[2] $Ks_{2MASS} = K_{SAAO} - (0.024 \pm 0.003) + (0.017 \pm 0.006)(J\text{-}K)_{SAAO}$.

We converted the *Ks*-band magnitudes to absolute magnitudes using the respective parallax given in Table 1 and estimated the mass for a given star. From the mass and radius, we were also able to calculate the surface gravity ($\log g$):

$$g_\star = \frac{GM_\star}{R_\star^2}, \quad (5)$$

where G is the gravitational constant. Table 2 shows a summary of the calculated mass, luminosity, and $\log g$ for our sample.

4 DISCUSSION

In order to discuss the behaviour of our sample stars, we investigate some relations between the available parameters. In the following analysis we also added stars from Mann et al. (2015) that have measured *Gaia* DR2 parallaxes (Gaia Collaboration 2018). In order to avoid contamination, the population from Mann et al. (2015) has further been cleaned by removing double stars and variable stars (as e.g. BY-Dra type). We start by constructing a relation between the stellar radius and stellar mass (MR relation) shown in Fig. 3. As pointed out by Mann et al. (2018), comparing their MLR to the one from Benedict et al. (2016) resulted in a discrepancy of more than 10 per cent for stars with masses $>0.3\,M_\odot$. This discrepancy is also visible in Fig. 3, where the black dots represent the masses

[2] http://www.astro.caltech.edu/~jmc/2mass/v3/transformations/

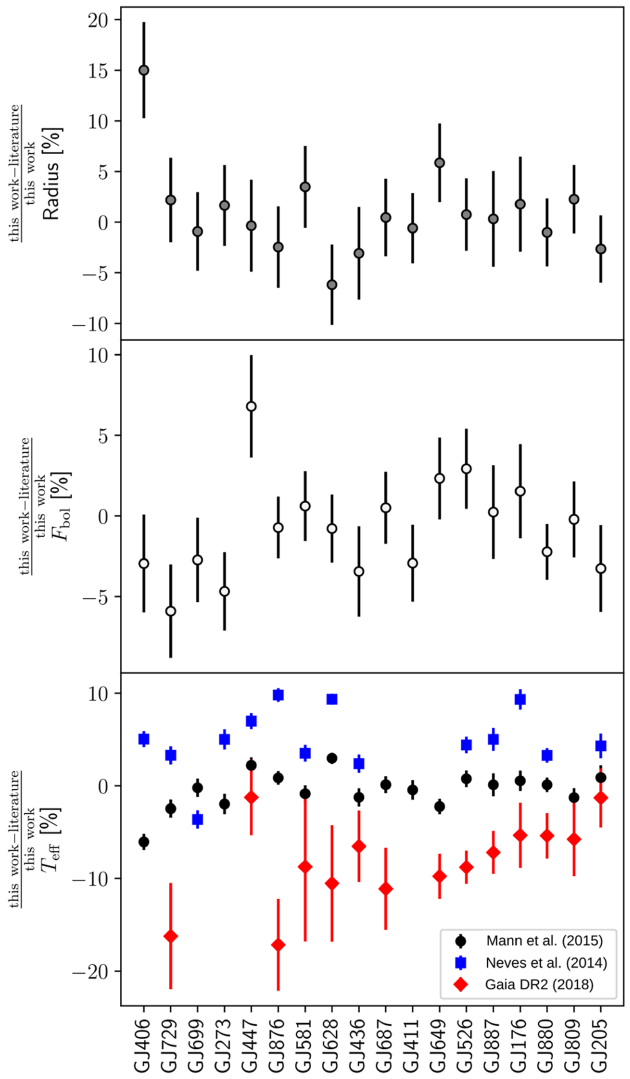

Figure 2. We compare our calculated radius, $F_{\rm bol}$, and $T_{\rm eff}$ with the ones from Mann et al. (2015). Stars are ordered according to our calculated $T_{\rm eff}$ from low (left-hand side) to high (right-hand side) temperature. The difference between the estimates is small, the mean difference for the radius is 2.9 per cent, $F_{\rm bol}$ is 2.5 per cent, and $T_{\rm eff}$ is 1.4 per cent. However, by comparing our $T_{\rm eff}$ with the ones from optical spectroscopy (Neves et al. 2014), we find an higher mean difference of 5.4 per cent and −8.2 per cent for *Gaia* DR2 $T_{\rm eff}$. However, single $T_{\rm eff}$s from *Gaia* DR2 can have differences of up to ∼15 per cent (see Section 3.4 for details).

calculated using the MLR relation from Mann et al. (2018) and the grey dots using Benedict et al. (2016). Above 0.3 $M_\odot$ we get higher masses for the same star using Benedict et al. (2016) compared to Mann et al. (2018). We also fitted polynomials of different degrees to each relation using the Levenberg–Marquardt algorithm. For each polynomial, we calculated the Akaike information criterion (AIC; Akaike 1974) and the Bayesian Information criterion (BIC; Schwarz 1978). We found that by using the MLR relation from Mann et al. (2018), the best-fitting polynomial for the MR relation is of third order, whereas by using Benedict et al. (2016), it is a fifth-order polynomial. The high-order structure caused by the MLR from Benedict et al. (2016) is also visible in Fig. 3. Since Mann et al. (2018) has been calibrated using accurate *Gaia* DR2 parallaxes, we continue to use their relation. We find that in this case, the mass–radius relation is best characterized by a cubic order polynomial of the form

$$\frac{R_\star}{\mathrm{R}_\odot} = 0.013(\pm0.010) + 1.238(\pm0.117)\,\frac{M_\star}{\mathrm{M}_\odot} - 1.13(\pm0.40)\left(\frac{M_\star}{\mathrm{M}_\odot}\right)^2 + 1.21(\pm0.42)\left(\frac{M_\star}{\mathrm{M}_\odot}\right)^3. \quad (6)$$

The standard deviation of the residuals is 0.016 $\mathrm{R}_\odot$ and the median absolute deviation (MAD) is 0.008 $\mathrm{R}_\odot$. The errors of the polynomial coefficients (closed brackets) are estimated from the covariance matrix.

We also establish a relation between the stellar radius and its effective temperature (see Fig. 4). Interestingly, in Fig. 4 we identified a discontinuous behaviour between 3200 and 3340 K (grey shaded area), where the radius spans a range from 0.18 to 0.42 $\mathrm{R}_\odot$ for similar effective temperatures. Considering that our mean measurement error for the radius is ∼0.006 $\mathrm{R}_\odot$, this corresponds to a 40σ difference. We also note that we have done a detailed error analysis of our diameter measurements in Lachaume et al. (2019). We further find that this discontinuity corresponds to a mass of 0.23 $\mathrm{M}_\odot$ (see the filled and empty dots in Fig. 4).

To the $T_{\rm eff}$–$R_\star$ data we fitted two linear polynomials depending on the mass range, namely for stars with $M_\star \geq 0.23\,\mathrm{M}_\odot$ and $M_\star < 0.23\,\mathrm{M}_\odot$. We also tried higher-order polynomials, but found in both cases that the higher-order coefficients were consistent with zero. We conclude therefore, that for the two cases, the data are best described with two linear polynomials of the form

$$\frac{R_\star}{\mathrm{R}_\odot} = \begin{cases} -1.223(\pm0.085) + 2.700(\pm0.138)\,\frac{T_{\rm eff}}{T_{\rm eff,\odot}} \\ \quad \text{for } M_\star \geq 0.23\,\mathrm{M}_\odot, \\ -0.277(\pm0.060) + 0.869(\pm0.113)\,\frac{T_{\rm eff}}{T_{\rm eff,\odot}} \\ \quad \text{for } M_\star < 0.23\,\mathrm{M}_\odot. \end{cases} \quad (7)$$

The standard deviations of the residuals are 0.051 $\mathrm{R}_\odot$ for $M_\star \geq 0.23\,\mathrm{M}_\odot$ and 0.016 $\mathrm{R}_\odot$ for $M_\star < 0.23\,\mathrm{M}_\odot$ and the respective MADs are 0.033 $\mathrm{R}_\odot$ and 0.0107 $\mathrm{R}_\odot$. In Fig. 5 we show the residuals after subtracting equation (7) as a function of metallicity. The slope in the data indicates a correlation between metallicity and radius; hence, we calculated the Pearson's correlation coefficient (r). For stars with $\mathrm{M}_\odot \geq 0.23$ we get $r = 0.69$ and for $\mathrm{M}_\odot < 0.23$ $r = 0.51$, respectively. We found that stars with higher metallicity have slightly larger radii and sub-solar metallicity stars lower radii. This correlation is strong for partially convective stars and moderate for fully convective ones. Burrows et al. (2007) proposed that enhanced opacity in atmospheres due to enhanced metallicity could cause inflated radii in giant planets. Given that we find a correlation between metallicity and radius, it is possible to have a similar effect in M-dwarfs. The metallicity effect on the radius can be best described by two linear polynomials of the form

$$\frac{\Delta R_\star}{R_\star} = \begin{cases} -0.0060(\pm0.0093) + 0.4166(\pm0.0462)\,[\mathrm{Fe/H}] \\ \quad \text{for } M_\star \geq 0.23\,\mathrm{M}_\odot, \\ 0.0187(\pm0.0176) + 0.2504(\pm0.0778)\,[\mathrm{Fe/H}] \\ \quad \text{for } M_\star < 0.23\,\mathrm{M}_\odot. \end{cases} \quad (8)$$

In Fig. 6 we show $T_{\rm eff}$–$R_\star$, where we corrected the stellar radius for possible metallicity effects using equation (8). The best-fitting

Table 2. Calculated other distance-dependent stellar parameters (see Section 3.5).

Star name	Ks (mag.)	M_{Ks} (mag.)	$M_\star$ ($M_\odot$)[a]	$L_\star$ ($L_\odot$)	log g (dex)
GJ1	4.53 ± 0.01[b]	6.33 ± 0.01	0.390 ± 0.010	0.0220 ± 0.0004	4.87
GJ176	5.63 ± 0.01[b]	5.74 ± 0.01	0.486 ± 0.011	0.0356 ± 0.0028	4.80
GJ205	3.86 ± 0.02[c]	5.08 ± 0.02	0.590 ± 0.015	0.0621 ± 0.0041	4.70
GJ273	4.87 ± 0.01[b]	6.97 ± 0.02	0.293 ± 0.007	0.0103 ± 0.0005	4.89
GJ406	6.15 ± 0.02[c]	9.13 ± 0.05	0.110 ± 0.003	0.0011 ± 0.0001	5.08
GJ411	3.36 ± 0.02[c]	6.33 ± 0.02	0.390 ± 0.010	0.0212 ± 0.0010	4.85
GJ436	6.04 ± 0.02[c]	6.09 ± 0.02	0.429 ± 0.010	0.0237 ± 0.0016	4.79
GJ447	5.68 ± 0.02[c]	8.04 ± 0.02	0.174 ± 0.004	0.0039 ± 0.0003	5.09
GJ526	4.56 ± 0.02[c]	5.89 ± 0.02	0.463 ± 0.011	0.0380 ± 0.0017	4.74
GJ551	4.38 ± 0.03[d]	8.81 ± 0.03	0.124 ± 0.003	0.0015 ± 0.0001	5.16
GJ581	5.85 ± 0.01[b]	6.85 ± 0.01	0.310 ± 0.007	0.0119 ± 0.0005	4.91
GJ628	5.09 ± 0.01[b]	6.92 ± 0.01	0.300 ± 0.007	0.0109 ± 0.0004	4.94
GJ649	5.63 ± 0.02[c]	5.55 ± 0.02	0.517 ± 0.013	0.0446 ± 0.0024	4.69
GJ674	4.86 ± 0.01[b]	6.57 ± 0.01	0.352 ± 0.008	0.0157 ± 0.0015	4.87
GJ687	4.50 ± 0.02[c]	6.21 ± 0.02	0.409 ± 0.010	0.0218 ± 0.0009	4.81
GJ699	4.53 ± 0.02[c]	8.23 ± 0.02	0.160 ± 0.004	0.0033 ± 0.0001	5.11
GJ729	5.39 ± 0.02[c]	8.03 ± 0.02	0.175 ± 0.004	0.0038 ± 0.0003	5.06
GJ809	4.58 ± 0.02[c]	5.34 ± 0.02	0.551 ± 0.014	0.0515 ± 0.0023	4.71
GJ832	4.46 ± 0.01[b]	5.98 ± 0.01	0.447 ± 0.011	0.0258 ± 0.0009	4.81
GJ876	5.04 ± 0.01[b]	6.69 ± 0.01	0.334 ± 0.008	0.0129 ± 0.0004	4.86
GJ880	4.54 ± 0.02[c]	5.36 ± 0.02	0.547 ± 0.014	0.0509 ± 0.0012	4.71
GJ887	3.33 ± 0.02[c]	5.74 ± 0.02	0.486 ± 0.012	0.0367 ± 0.0022	4.78

[a]Estimated using MLR from Mann et al. (2018) [b]Koen et al. (2010) [c]Mann et al. (2015) [d]Cutri et al. (2003)

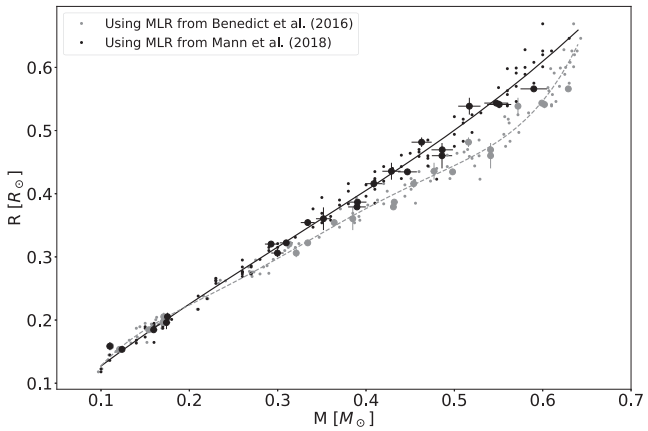

Figure 3. Radius–mass relation for our sample (large dots) and a subset of data from Mann et al. (2015; small dots) selected as described in the text. The black dots are based on mass estimates using the MLR from Mann et al. (2018) whereas grey dots are based on the one from Benedict et al. (2016). The lines show best-fitting polynomial as resulted from the respective MLR (the details are discussed in Section 4).

polynomials in this case are

$$\frac{R_\star}{\mathrm{R}_\odot} = \begin{cases} -1.169(\pm0.063) + 2.620(\pm0.103)\,\frac{T_{\rm eff}}{T_{\rm eff,\odot}} \\ \qquad \text{for } M_\star \geq 0.23\,\mathrm{M}_\odot, \\ -0.367(\pm0.050) + 1.041(\pm0.094)\,\frac{T_{\rm eff}}{T_{\rm eff,\odot}} \\ \qquad \text{for } M_\star < 0.23\,\mathrm{M}_\odot. \end{cases} \quad (9)$$

The standard deviations of the residuals are 0.038 $\mathrm{R}_\odot$ and 0.013 $\mathrm{R}_\odot$, respectively, which is slightly lower compared to neglecting the influence of metallicity on the radius. The MADs of the residuals are 0.029 $\mathrm{R}_\odot$ and 0.008 $\mathrm{R}_\odot$.

Based on our observations and our inferred physical parameters, we further show in Fig. 7 the empirical HR diagram for the two different mass populations. We can also identify a transition region in the HR diagram. We establish the following linear (log $L_\star$)–$T_{\rm eff}$ relation for the two different populations

$$\log L_\star = \begin{cases} -6.710(\pm0.179) + 8.318(\pm0.290)\,\frac{T_{\rm eff}}{T_{\rm eff,\odot}} \\ \qquad \text{for } M_\star \geq 0.23\,\mathrm{M}_\odot, \\ -6.856(\pm0.345) + 8.099(\pm0.653)\,\frac{T_{\rm eff}}{T_{\rm eff,\odot}} \\ \qquad \text{for } M_\star < 0.23\,\mathrm{M}_\odot. \end{cases} \quad (10)$$

4.1 Transition into the fully convective regime

Theoretical stellar evolution predicts a transition from partially convective stars into the fully convective stellar regime to occur at stellar mass somewhere between 0.2 $\mathrm{M}_\odot$ (Dorman et al. 1989) and 0.35 $\mathrm{M}_\odot$ (Chabrier & Baraffe 1997) depending on the underlying stellar model. While a partially convective star still resembles a sun-like structure, having a radiative zone and a convective envelope, fully convective stars have no such zone. Our observations indicate that the limit between partially and fully convective regime is around ≈0.23 $\mathrm{M}_\odot$ and between 3200 and 3340 K. The lack of a detection of this transition in previous works can be explained mainly by the fact that very few single M-dwarfs with temperatures below 3270 K have interferometrically measured radii. In fact, Boyajian et al. (2012a) shows only two M-dwarfs with temperatures below this value. Moreover, they include in their work mostly one of the stars (GJ 699) that is in the fully convective regime, as GJ 551 was excluded from most of their analyses. Another reason is that previous radius measurements of fully convective stars relied on eclipsing M-dwarf binaries, where the disentanglement of the respective components is not straightforward. Finally, most radius estimates rely on stellar evolution models rather than direct measurements, i.e. in many cases the radius has not been measured directly.

Furthermore, we find that the linear term of the polynomial in equation (7) shows a steeper slope for stars with $M_\star \geq 0.23\,\mathrm{M}_\odot$ than for $M_\star < 0.23\,\mathrm{M}_\odot$. This is possibly due to the fact that stars

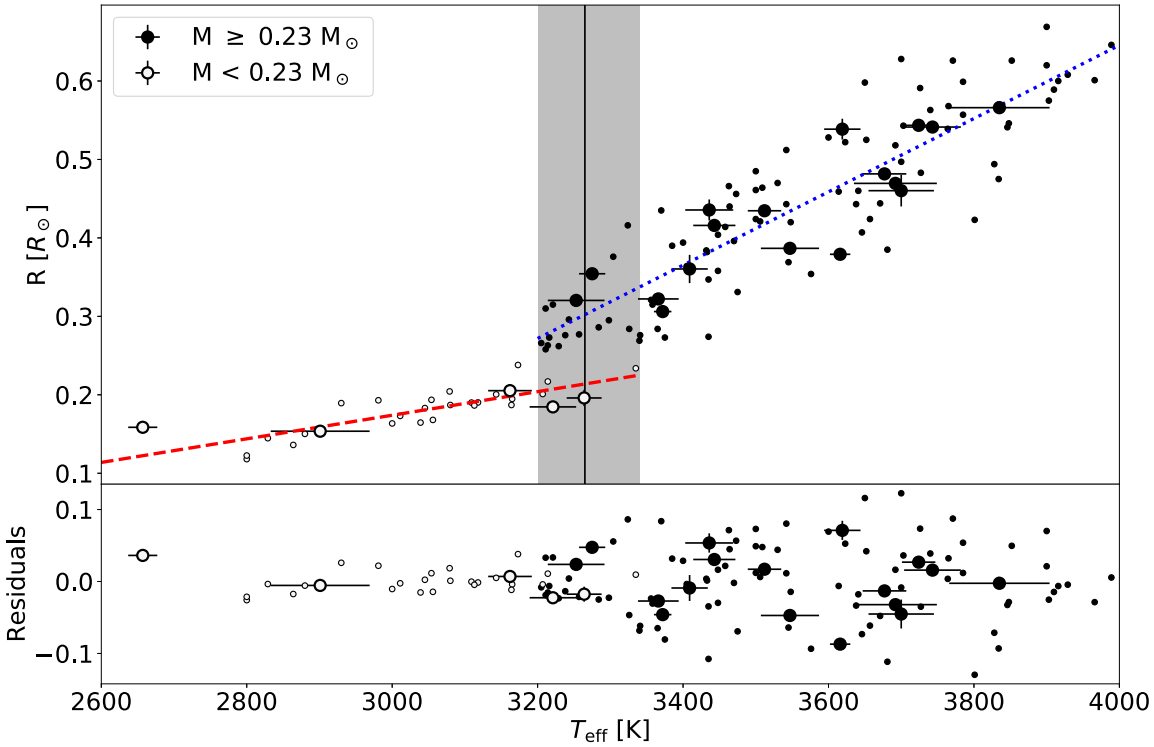

Figure 4. $T_{\rm eff}$ versus radius plot with the stellar mass coded as filled and empty circles, respectively. The lines show fitted polynomials for the two different mass populations (red dashed line for stars with masses $< 0.23\,{\rm M}_{\odot}$ and blue dotted line for stars with masses $\geq 0.23\,{\rm M}_{\odot}$). The grey shaded area shows the region where we find a possible discontinuity and which we attribute to the transition between partially and fully convective stars. We also added M-dwarfs from Mann et al. (2015; small dots), see the text for details. The lower plot shows the residual after subtracting the polynomials in equation (7) from the radius measurements (the details are discussed in Section 4).

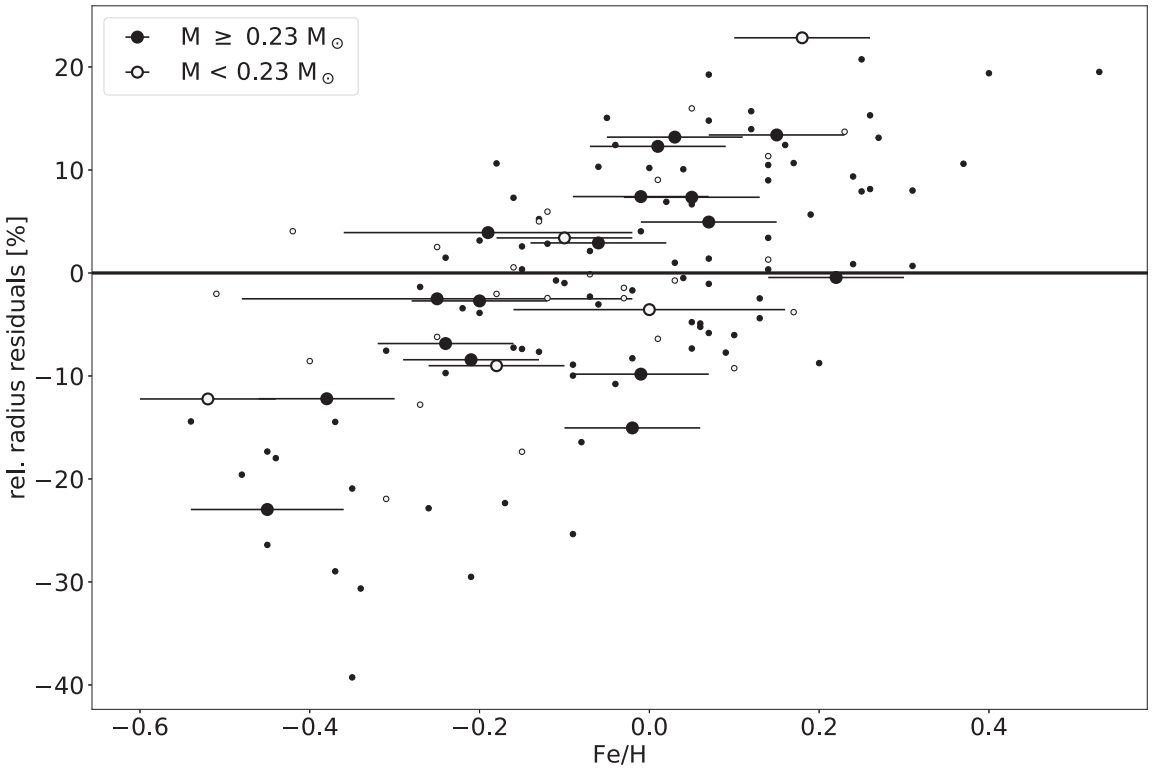

Figure 5. Residuals after subtracting equation (7) from the radius measurement as a function of stellar metallicity. The Pearson correlation coefficient is $r = 0.69$ for $M_{\star} \geq 0.23\,{\rm M}_{\odot}$ and $r = 0.51$ for $M_{\star} < 0.23\,{\rm M}_{\odot}$. The horizontal line represents the case of zero residuals (the details are discussed in Section 4).

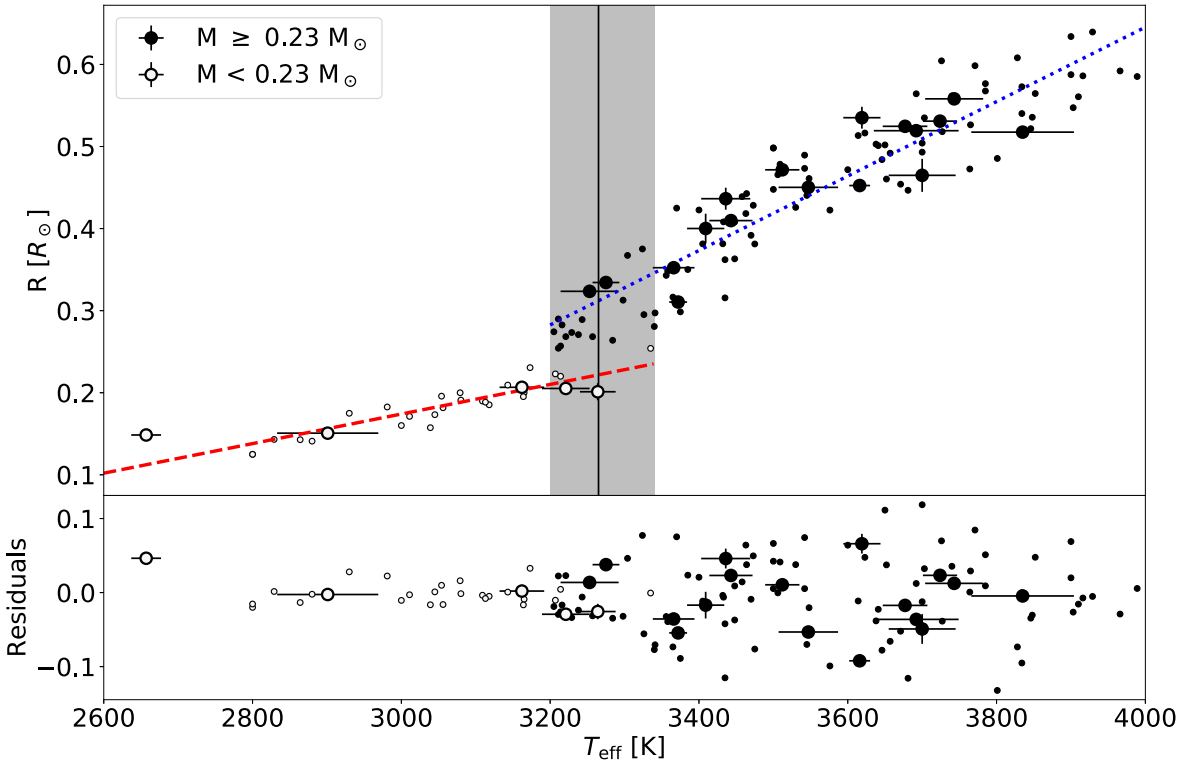

Figure 6. Same as Fig. 4 but correcting the radius for possible metallicity effects (the details are discussed in Section 4).

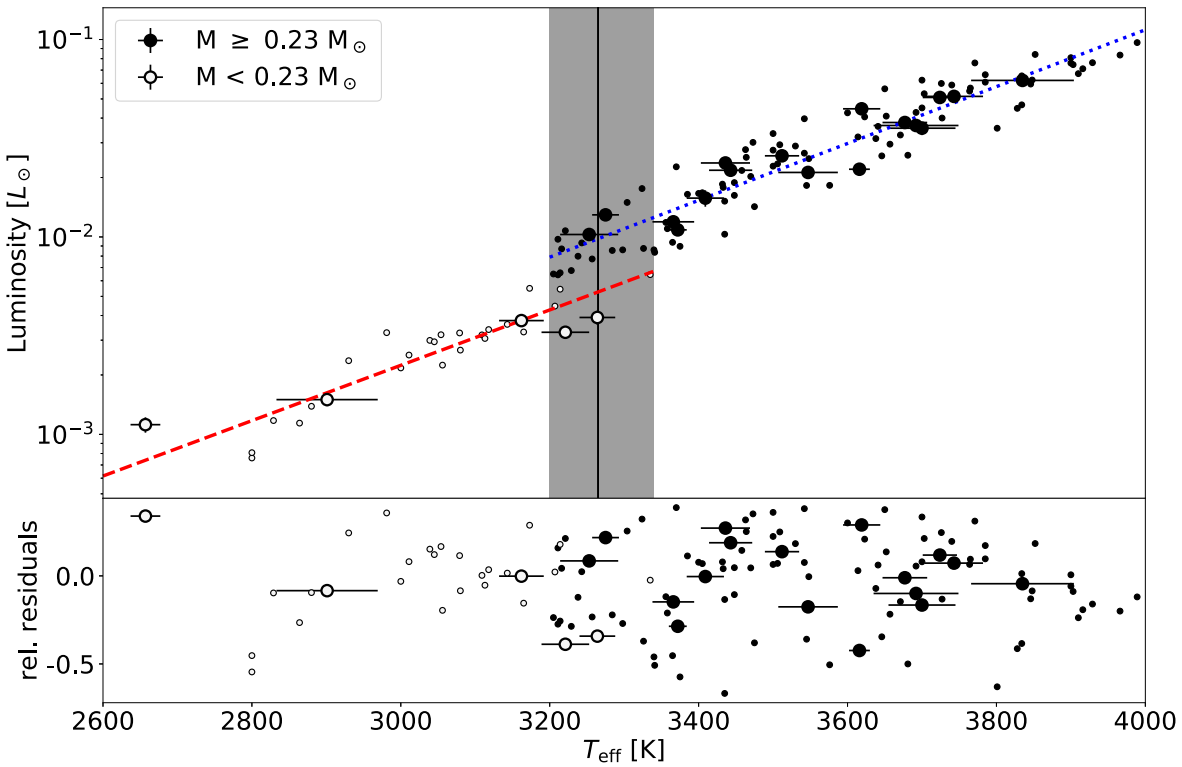

Figure 7. Empirical HR diagram for two different stellar mass populations (filled and empty circles, respectively). The red dashed line shows our fitted polynomials for stars with masses $< 0.23\,M_{\odot}$ and the blue dotted one for masses $\geq 0.23\,M_{\odot}$. We identify a discontinuity (grey shaded area) reflecting the transition region between partially and fully convective stars. Our sample is depicted by the large dots. The sample from Mann et al. (2015) is represented by the smaller dots, which also have their error bars suppressed. Lower plot shows the relative residuals after subtracting equation (10) from the luminosity value $(\frac{\text{calc. luminosity}-\text{polynomial}}{\text{calc. luminosity}})$ (the details are discussed in Section 4).

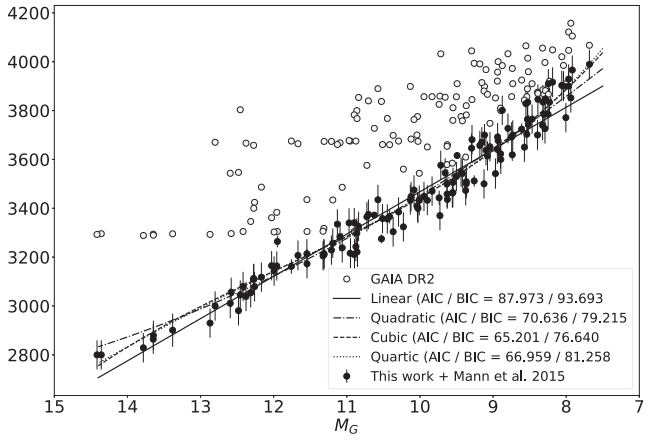

Figure 8. Effective temperature as a function of absolute *Gaia* G magnitude. The empty circles show $T_{\rm eff}$ estimated by *Gaia* DR2 Apsis. The filled dots show our measurements and the ones from Mann et al. (2015). Lines show polynomial fits of different orders. Their respective AIC and BIC values are given in the legend (the details are discussed in Section 4.2).

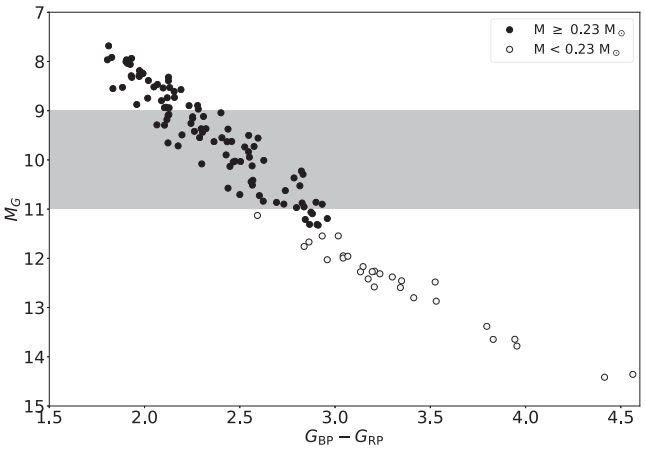

Figure 9. Absolute *Gaia* G magnitude versus $G_{\rm BP} - G_{\rm RP}$ for M-dwarfs with different masses. The grey shaded area shows the region where Jao et al. (2018) found a gap in their HR diagram (the details are discussed in Section 4.2).

with $M_\star \geq 0.23\,{\rm M}_\odot$ still have a radiative zone that decreases with shrinking $T_{\rm eff}$. For M-dwarfs with $M_\star < 0.23\,{\rm M}_\odot$ the stars are fully convective, i.e. the convective zone extends towards the core. Therefore, the linear term for M-dwarfs with masses below $0.23\,{\rm M}_\odot$ indicates a more flattened slope. The gentle slope for masses below $0.23\,{\rm M}_\odot$ is consistent with the fact that fully convective stars have similar spectral types due to H_2 formation, which also flattens the radius–temperature relation (Chabrier & Baraffe 2000).

4.2 M-dwarfs in the context of *Gaia*

In Section 3.4 we noticed a considerable difference between $T_{\rm eff}$ for M-dwarfs inferred from *Gaia* three-band photometry (Andrae et al. 2018) and estimates found here and in the literature (Neves et al. 2014; Mann et al. 2015). Therefore, we establish an empirical calibration relation for stars with very well measured G magnitudes and parallaxes from *Gaia*. We use these two measurements to calculate the absolute G magnitude $M_{\rm G}$, which we relate to the $T_{\rm eff}$. In Fig. 8 we show $T_{\rm eff}$ as a function of $M_{\rm G}$. The empty circles show the stellar $T_{\rm eff}$ as estimated by *Gaia* Apsis, whereas the filled circles show our $T_{\rm eff}$ measurements and the ones from Mann et al. (2015). The previously shown discrepancy is also visible in Fig. 8. We determine an empirical relation to obtain $T_{\rm eff}$ from $M_{\rm G}$. In our attempt to find the best relation, we fitted polynomials of different degrees and we calculated their respective AIC and BIC (see Fig. 8). The best relation is described by a cubic polynomial of the form

$$T_{\rm eff} = 10171.7(\pm1449.6) - 1493.4(\pm410.8)M_{\rm G} + 114.1(\pm38.3)M_{\rm G}^2 - 3.2(\pm1.2)M_{\rm G}^3. \quad (11)$$

The standard deviation of the residuals is 53 $T_{\rm eff}$ and the MAD 36 $T_{\rm eff}$. The errors of the polynomial coefficients (closed brackets) are estimated from the covariance matrix.

Recently, Jao et al. (2018) presented an investigation showing an ∼0.05 mag gap in the HR diagram constructed from M-dwarfs using the *Gaia* DR2. The authors attributed this gap to a possible transition from partially to fully convective low-mass stars. However, recent simulations by MacDonald & Gizis (2018) argued that this gap can be explained by ^{3}He instabilities of low-mass stars rather than the before-mentioned transition region. This ^{3}He instabilities are caused by stars with a thin radiative zone, slightly above the transition to fully convective stars. These instabilities can produce energy fluctuations and a dip in the luminosity function (van Saders & Pinsonneault 2012; MacDonald & Gizis 2018). In Fig. 9 we show $M_{\rm G}$ over $G_{\rm BP} - G_{\rm RP}$ and mark the region where Jao et al. (2018) found their discontinuity (grey shaded area). The locus of our discovered discontinuity is slightly below the one from Jao et al. (2018). This increases the likelihood of the finding from MacDonald & Gizis (2018) and our claim having observed the transition region between fully and partially convective stars, which should occur slightly below the ^{3}He instability region.

5 CONCLUSION

We have measured physical parameters of 13 M-stars covering the partially and fully convective regime using interferometric measurements from the VLTI and parallaxes from *Gaia* DR2. Our measurements extend to lower $T_{\rm eff}$ than previous interferometric studies, and we use them augmented with literature data to present improved empirical relations between stellar radius and mass, and between stellar radius and luminosity as a function of $T_{\rm eff}$. Analysing residuals to our relations, we identified a general trend that late-type stars with higher metallicity are slightly inflated, whereas for stars with lower metallicity we measure predominantly smaller radii. We find this correlation to be strong for stars with $M_\star \geq 0.23\,{\rm M}_\odot$ and moderate for $M_\star < 0.23\,{\rm M}_\odot$, respectively. We also found that *Gaia* $T_{\rm eff}$ values are significantly underestimated (≈8 per cent) for M-dwarfs.

The most striking feature we identified in our data is a sharp transition in the relation between $R_\star$ and $T_{\rm eff}$, as well as in the empirical HR diagram, which we identify as reflecting the transition between partially and fully convective stars. While previously only a hint for this change had been inferred indirectly, we now have a possible direct observation. We showed that this change happens at $\sim 0.23\,{\rm M}_\odot$ and between 3200 and 3340 K. In this region, we measure radii in the range from 0.18 to 0.42 $R_\odot$. Thus, our findings put strong constraints on the stellar evolution and interior structure models.

ACKNOWLEDGEMENTS

We thank the reviewer for their helpful comments on the manuscript. MR acknowledges support from CONICYT project Basal AFB-170002. Partially based on observations obtained via ESO under program IDs 090.D-0917, 091.D-0584, 092.D-0647, 093.D-0471. AJ acknowledges support from FONDECYT project 1171208, CONICYT project BASAL AFB-170002, and by the Ministry for the Economy, Development, and Tourism's Programa Iniciativa Científica Milenio through grant IC 120009, awarded to the Millennium Institute of Astrophysics (MAS). RB acknowledges additional support from project IC120009 'Millenium Institute of Astrophysics (MAS)' of the Millennium Science Initiative, Chilean Ministry of Economy. This work made use of the Smithsonian/NASA Astrophysics Data System (ADS) and of the Centre de Données astronomiques de Strasbourg (CDS). This research made use of ASTROPY, a community-developed core PYTHON package for Astronomy (ASTROPY Collaboration, 2013). This work has made use of data from the European Space Agency (ESA) mission *Gaia* (https://www.cosmos.esa.int/gaia), processed by the *Gaia* Data Processing and Analysis Consortium (DPAC; https://www.cosmos.esa.int/web/gaia/dpac/consortium). Funding for the DPAC has been provided by national institutions, in particular the institutions participating in the *Gaia* Multilateral Agreement.

REFERENCES

Akaike H., 1974, IEEE Trans. Autom. Control, 19, 716
Andrae R. et al., 2018, A&A, 616, A8
Benedict G. F. et al., 2016, AJ, 152, 141
Berger D. H. et al., 2006, ApJ, 644, 475
Bonfils X. et al., 2013, A&A, 549, A109
Boyajian T. S. et al., 2012a, ApJ, 757, 112
Boyajian T. S. et al., 2012b, ApJ, 757, 112
Browning M. K., 2008, ApJ, 676, 1262
Buchner J. et al., 2014, A&A, 564, A125
Burrows A., Hubeny I., Budaj J., Hubbard W. B., 2007, ApJ, 661, 502
Chabrier G., Baraffe I., 1997, A&A, 327, 1039
Chabrier G., Baraffe I., 2000, ARA&A, 38, 337
Cutri R. M. et al., 2003, 2MASS All Sky Catalog of point sources
Demory B.-O. et al., 2009, A&A, 505, 205
Donati J.-F. et al., 2008, MNRAS, 390, 545
Dorman B., Nelson L. A., Chau W. Y., 1989, ApJ, 342, 1003
Dressing C. D., Charbonneau D., 2013, ApJ, 767, 95
Espinoza N., Jordán A., 2015, MNRAS, 450, 1879
Feroz F., Hobson M. P., 2008, MNRAS, 384, 449
Gaia Collaboration 2018, A&A, 616, A1
Gallenne A. et al., 2018, A&A, 616, A68
Hanbury Brown R., Davis J., Lake R. J. W., Thompson R. J., 1974, MNRAS, 167, 475
Husser T. O., Wende-von Berg S., Dreizler S., Homeier D., Reiners A., Barman T., Hauschildt P. H., 2013, A&A, 553, A6
Irwin J., Berta Z. K., Burke C. J., Charbonneau D., Nutzman P., West A. A., Falco E. E., 2011, ApJ, 727, 56
Jao W.-C., Henry T. J., Gies D. R., Hambly N. C., 2018, ApJ, 861, L11
Kesseli A. Y., Muirhead P. S., Mann A. W., Mace G., 2018, AJ, 155, 225
Koen C., Kilkenny D., van Wyk F., Marang F., 2010, MNRAS, 403, 1949
Kopparapu R. K., 2013, ApJ, 767, L8
Lachaume R., Rabus M., Jordan, A., Brahm R., Boyajian T., von Braun K., Berger, J.-P., 2019, preprint (arXiv:1901:02879)
Lachaume R., Rabus M., Jordán A., 2014, in Rajagopal J. K., Creech-Eakman M. J., Malbet F., eds, Proc. SPIE Conf. Ser. Vol. 9146, Optical and Infrared Interferometry IV. SPIE, Bellingham, p. 914631
Le Bouquin J. B. et al., 2011, A&A, 535, A67
MacDonald J., Gizis J., 2018, MNRAS, 480, 1711
Mann A. W., Feiden G. A., Gaidos E., Boyajian T., von Braun K., 2015, ApJ, 804, 64
Mann A. W., von Braun K., 2015, PASP, 127, 102
Mann A. W. et al., 2018, preprint (arXiv:1811.06938)
Neves V., Bonfils X., Santos N. C., Delfosse X., Forveille T., Allard F., Udry S., 2014, A&A, 568, A121
Newton E. R., Irwin J., Charbonneau D., Berta-Thompson Z. K., Dittmann J. A., West A. A., 2016, ApJ, 821, 93
Ricker G. R. et al., 2014, in Oschmann J. M. Jr, Clampin M., Fazio G. G., MacEwen H. A., eds, Proc. SPIE Conf. Ser. Vol. 9143, Space Telescopes and Instrumentation 2014: Optical, Infrared, and Millimeter Wave. SPIE, Bellingham, p. 914320
Schwarz G., 1978, Ann. Stat., 6, 461
Skilling J., 2004, in Fischer R., Preuss R., Toussaint U. V., eds, AIP Conf. Ser. Vol. 735, Bayesian Inference and Maximum Entropy Methods in Science and Engineering. Am. Inst. Phys., New York, p. 395
Ségransan D., Kervella P., Forveille T., Queloz D., 2003, A&A, 397, L5
van Belle G. T., van Belle G., 2005, PASP, 117, 1263
van Saders J. L., Pinsonneault M. H., 2012, ApJ, 751, 98
von Braun K. et al., 2011, ApJ, 729, L26
von Braun K. et al., 2012, ApJ, 753, 171
von Braun K. et al., 2014, MNRAS, 438, 2413
Wright N. J., Drake J. J., 2016, Nature, 535, 526

This paper has been typeset from a TEX/LATEX file prepared by the author.